



HAL
open science

Tuning the Tin Oxide-Carbon Composite Support to Deposit Rh Nanoparticles for Glycerol-to-Carbonate Electro-Conversion

Thamyres F M Moreira, Guilherme B Bresciani, K. Boniface Kokoh, Teko W Napporn, Paulo Olivi, Cláudia Morais

► **To cite this version:**

Thamyres F M Moreira, Guilherme B Bresciani, K. Boniface Kokoh, Teko W Napporn, Paulo Olivi, et al.. Tuning the Tin Oxide-Carbon Composite Support to Deposit Rh Nanoparticles for Glycerol-to-Carbonate Electro-Conversion. *Journal of The Electrochemical Society*, 2022, 169 (9), pp.094502. 10.1149/1945-7111/ac908d]. hal-03875810

HAL Id: hal-03875810

<https://hal.science/hal-03875810>

Submitted on 28 Nov 2022

HAL is a multi-disciplinary open access archive for the deposit and dissemination of scientific research documents, whether they are published or not. The documents may come from teaching and research institutions in France or abroad, or from public or private research centers.

L'archive ouverte pluridisciplinaire **HAL**, est destinée au dépôt et à la diffusion de documents scientifiques de niveau recherche, publiés ou non, émanant des établissements d'enseignement et de recherche français ou étrangers, des laboratoires publics ou privés.

OPEN ACCESS

Tuning the Tin Oxide-Carbon Composite Support to Deposit Rh Nanoparticles for Glycerol-to-Carbonate Electro-Conversion

To cite this article: Thamyres F. M. Moreira *et al* 2022 *J. Electrochem. Soc.* **169** 094502

View the [article online](#) for updates and enhancements.



 The Electrochemical Society
Advancing solid state & electrochemical science & technology

243rd ECS Meeting with SOFC-XVIII

More than 50 symposia are available!






Present your research and accelerate science

Boston, MA • May 28 – June 2, 2023

[Learn more and submit!](#)



Tuning the Tin Oxide-Carbon Composite Support to Deposit Rh Nanoparticles for Glycerol-to-Carbonate Electro-Conversion

Thamyres F. M. Moreira,^{1,2,z}  Guilherme B. Bresciani,¹ K. Boniface Kokoh,^{2,*z}  Teko W. Napporn,^{2,*}  Paulo Olivi,¹  and Cláudia Morais^{2,z} 

¹Laboratório de Eletroquímica e Eletrocatalise Ambiental, Departamento de Química da Faculdade de Filosofia Ciências e Letras de Ribeirão Preto, Universidade de São Paulo, Av. Bandeirantes, 3900, 14040-901 Ribeirão Preto, SP, Brazil

²Université de Poitiers, IC2MP, UMR CNRS 7285, 4, rue Michel Brunet, B27, TSA 51106, 86073 Poitiers Cedex 09, France

Glycerol Electrooxidation Reaction (GEOR) has been herein investigated on Rh/C and Rh/SnO₂-C prepared by polyol method. The particle mean sizes were found to be 2.0 and 1.8 nm in Rh/C and Rh/SnO₂-C, respectively. The alloying degree reached 63% in Rh/SnO₂-C, confirming a Sn-Rh alloy formation. The activity towards GEOR on Rh/SnO₂-C was almost 5-fold higher than on Rh/C, as demonstrated by electrochemical measurements in alkaline medium. This trend indicated the beneficial effect of the SnO₂-C carbon-oxide composite support in the catalyst composition. Analysis of the products generated after the bulk electrolysis using high-performance liquid chromatography (HPLC) and FTIRS demonstrated that at 0.55 V vs RHE the main reaction products were glycerate ion and carbonate (CO₃²⁻). Then, a C–C cleavage was demonstrated with the CO₃²⁻ formation at low potentials. During the testings conducted in a home-made acrylic direct glycerol fuel cell at room temperature in 0.5 mol l⁻¹ NaOH, the maximum power density (390 μW cm⁻²) obtained on a Rh/SnO₂ anode, was 5-fold higher than that on Pd/C. These testings demonstrated that the co-generation of sustainable energy and value-added products is a promising way to valorize glycerol.

© 2022 The Author(s). Published on behalf of The Electrochemical Society by IOP Publishing Limited. This is an open access article distributed under the terms of the Creative Commons Attribution 4.0 License (CC BY, <http://creativecommons.org/licenses/by/4.0/>), which permits unrestricted reuse of the work in any medium, provided the original work is properly cited. [DOI: 10.1149/1945-7111/ac908d]



Manuscript submitted June 29, 2022; revised manuscript received August 24, 2022. Published September 16, 2022.

Supplementary material for this article is available [online](#)

Direct Alcohol Fuel Cells (DAFCs) have been extensively studied as power sources for mobile, stationary and portable applications.¹ Efficient electrochemical energy conversion in DAFCs is a sustainable and environmentally friendly alternative to decrease fossil fuel dependence in the society.² Recently, C₂ and C₃-alcohols have been used as fuel in DAFCs resulting in substantial study interests, especially due to less toxicity, low cost, and easy transportation.^{3,4} In particular, glycerol utilization and its valorization as fuel appear to be a very attractive process due to its large availability.^{5,6} The recent biodiesel production growth increased glycerol accumulation as a waste side-product of this process, and it is estimated that each 10 kg of biodiesel leads to 1 kg of glycerol.⁷ Brazil is the second world biodiesel producer with several fabrication processes using different materials, such as animal fat, sunflowers oil, waste oil from frying, among others.⁵ Consequently, the glycerol valorization interest explores several catalytic routes such as electrochemical, alcohol reforming, additives development, and biotechnological.^{8–11} The electrochemical route is very attractive, and many studies indicate that this double process in one so called cogeneration allows to valorize glycerol into energy source, while producing molecules with added value.^{6,8,12–15} As example, Nahay et al.¹⁶ studied the Direct Glycerol Fuel Cell (DGFC) performance using a palladium-gold (PdAu/C) electrocatalyst in the anode compartment, reaching 7.0 mW cm⁻² power density. Recently, Chin Liu et al.¹⁷ studied the Glycerol Electrochemical Oxidation Reaction (GEOR) on copper oxide (CuO), which resulted in a high selectivity towards dihydroxyacetone (DHA) considered as extremely valuable in the fine chemical and pharmaceutical industries.¹⁸

Concerning power source applications, the main development challenge of DGFCs remains in the anode kinetics process. This highlights thus the need to design an electrode material that is both more efficient and durable, i.e., more active and stable over multiple uses.^{19,20} Platinum (Pt) and Pd based catalysts are widely studied as anode catalysts in DGFCs.^{14,18,21–27} However, different approaches for non-Pt and -Pd metal catalysts development and prospects have been discussed. Houache et al.²⁸ prepared nickel (Ni) based catalysts

for GEOR in alkaline medium and concluded that glyceraldehyde was the main reaction product. Zhang et al.²⁹ studied the Au/C anode catalyst performance in DGFC and obtained a 57.9 mW cm⁻² peak power density at 80 °C. They concluded that Au/C promoted tartrate, mesoxalate and oxalate formation, and enhanced the Faradaic efficiency in a glycerol fuel cell.

Rhodium (Rh) is considered as a promising anode material in ethanol oxidation reaction (EOR) investigations since it is known to promote the C–C bond cleavage at low potentials.^{30–33} At the same time, there are not enough reports addressing GEOR. For example, X. Lam et al.³⁴ prepared Rh supported on carbon black and evaluated its performance in an alkaline medium. The onset and peak potential were observed to be more negative than those on Pt/C and Pd/C catalysts, but the GEOR current density remained lower. Therefore, it is necessary to improve the catalytic activity to overcome this issue. Some authors proposed the support material modification using different compositions such as graphene, carbon nanotubes, and oxide-carbon composites.^{24,26,35} The oxide-carbon composites as support material for electrocatalysts have particularly gained attention, mainly due to enhancements in the catalytic properties in noble metals catalysts such as high oxidation resistance, metal-support interaction that modifies the electronic effect, and stability properties of the catalytic center.^{36–39} Matsubu et al.⁴⁰ investigated the oxide composite supports –TiO₂ and Nb₂O₅– effects on Rh catalysts applied to the CO₂ reduction process. The main effect was evaluated using in situ spectroscopy and microscopy, showing that the catalysts have increased CO₂-reduction selectivity. Another important reported oxide-carbon composite is tin oxide (SnO₂) incorporated with carbon (C). Studies demonstrated that this combination is effective to upgrade the electrochemical properties of SnO₂ electrodes.⁴¹ The main benefit of carbon oxide composite addition is related to the increase in electronic conductivity, which facilitates the electron and ion transports, consequently, enhancing the catalytic performance.^{37,42–44} Soares et al.³⁰ investigated the SnO₂-C composite effect in the EOR on Pt-Rh catalysts. It was noticed that the SnO₂ promoted the ethanol electro conversion in acidic medium due to the ligand effect and the bifunctional mechanism combination. However, more contributions are still necessary to understand the beneficial effects of using oxide-carbon composites on Rh monometallic catalysts, especially for GEOR.

*Electrochemical Society Member.

^zE-mail: thamyres.moreira@alumni.usp.br; claudia.gomes.d.morais@univ-poitiers.fr; boniface.kokoh@univ-poitiers.fr

The catalytic properties enhancement also depends on the chosen synthesis method.^{45–47} That is because, size, dispersity, porosity, and nanoparticles surface area are parameters directly related to the synthesis route.^{6,48–50} In terms of applicability, designing high-performance electrocatalysts is considered one of the main concerns in DGFCs technology.^{48,51} In this context, the polyol method has several advantages in nanoparticles fabrication, such as good crystallinity and controlled particle growth, short preparation time, low cost, and simple process steps.^{52,53} Herein the synthesis protocol consists in using polyalcohol as a reducing agent and solvent, namely ethylene glycol (EG), which presents a high boiling point (197 °C), leading to increase the solubility of the inorganic precursor salts.^{48,54} Furthermore, this route facilitates experimental conditions optimization for addressing an easy metallic precursor reduction.^{55,56} For Rh nanoparticles synthesis, the polyol method appears as an interesting approach.⁵⁷ Zhang et al.⁵⁸ used a simple optimized polyol method to prepare Rh nanocubes for the pyrrole hydrogenation and CO oxidation. Kim et al.⁵⁹ investigated the Rh nanoparticles prepared by polyol method for CO hydrogenation and C2-higher alcohols production.

Based on all these previous studies, the main goal of the present study is the evaluation of Rh/C and Rh/SnO₂-C composite materials performances in GEOR in alkaline medium. For this purpose, Rh nanoparticles were deposited onto the conductive support by polyol method and the performance in DGFC was tested in a home-made acrylic cell. The reaction intermediates and the main products issued from the GEOR were identified by in situ Fourier transform infrared spectroscopy (FTIRS) and quantified by high-performance liquid chromatography (HPLC) coupled with an ultraviolet-visible (UV-vis) detector followed by a refractive index detector (RID).

Experimental

Chemicals.—Rhodium chloride (RhCl₃·xH₂O, 38%–40% Rh basis), glycerol (ReagentPlus > 99%), ethylene glycol (EG), propylene glycol (PG), citric acid (CA), and sodium hydroxide (NaOH, 97%) were purchased from Sigma-Aldrich and used as received. Carbon Vulcan XC 72 R from Cabot was added to the synthesis solution for Rh/C catalyst and in SnO₂-C oxide-carbon composite support. Carbon Vulcan was submitted to heat treatment in a tubular oven (MAITEC) operating at 900 °C under argon atmosphere for 5 h.³⁰ The catalytic ink formulation was conducted using Isopropanol and Nafion[®] 1100 EW wt.5% suspension, in a mixture of aliphatic alcohols and water, both purchased from Merck. Carbon Toray paper was purchased from FuelCellStore and used as a support onto which anode and cathode inks were deposited to prepare the homemade DGFC. The chromatographic analyses (HPLC) were conducted by internal calibration; this required purchasing (from Sigma-Aldrich) all the molecules likely to be formed from the glycerol oxidation investigation, i.e., tartronic, glyceric, glycolic, glyoxylic, oxalic and formic acids, and sodium carbonate. Millipore Milli-Q[®] water (18.2 MΩ cm at 20 °C) was used in all prepared solutions.

Catalysts synthesis.—Several methods are reported to prepare SnO₂ oxide.^{37,38,44} However, the thermal decomposition of the polymeric precursors (DPP) synthesis route, also called-Pechini method, is considered as a suitable oxide preparation approach.^{60,61} Therefore, in order to produce the SnO₂ the first step was the tin precursor solution preparation.⁶² Thus, the tin citrate solution was dissolved in EG and citric acid mixture under constant stirring at 90 °C–95 °C. The metal/citric acid/ethylene glycol molar ratio was 1:4:16, respectively. Then, the resulting solution was heated to 90 °C for 4 h. The tin precursor solution concentration was determined by gravimetric analysis. Finally, the SnO₂-C composite was synthesized by adding an appropriate amount of precursor solution and carbon Vulcan XC-72R followed by a calcination process at 325 °C for 2 h. The SnO₂ and C proportions in the composite support (30 and 70% m m⁻¹, respectively) were chosen

from previous investigations in our research group.³⁰ The resulting composite was characterized by thermogravimetric analysis (TGA) and X-ray diffraction (XRD).

The catalyst preparation was inspired by the polyol method optimized by González-Quijano research group.⁶³ Firstly, rhodium chloride (RhCl₃·xH₂O, 38%–40% Rh basis) was dissolved in 2.0 ml of ethanol. Then, carbon Vulcan or the composite material were mixed with 100 ml EG in an ultrasound bath for 30 min; and the Rh solution freshly prepared was added into the resulting solution. The system (Rh/C or Rh/SnO₂-C) was maintained under continuous stirring for 1 h and, sequentially, the pH was adjusted to 12 using 1.0 mol l⁻¹ NaOH. Afterwards, the temperature was increased up to 130 °C and the solution was under continuous stirring for 3 h. When the solution was at room temperature, its pH was adjusted to 2 with 1 mol l⁻¹ H₂SO₄. The mixture was the stirred for 3 h and finally, the resulting catalytic powder was recovered by filtration, abundant rinsing and then drying at 40 °C for 12 h. The Pt/C and Pd/C materials were also prepared following the same procedure for comparing the findings, especially in voltage cell performances. All the catalysts were prepared keeping a 20 wt.% metal loading. The characterization was performed using XRD, transmission electron microscopy (TEM), CO stripping and cyclic voltammetric (CV) measurements.

Physicochemical characterization.—The SnO₂-C proportion was confirmed by thermogravimetric analysis (TGA) performed on a Q600 TA Instruments SDT2960 under synthetic air using a 10 °C min⁻¹ heating rate from 20 to 900 °C. The X-ray diffraction patterns of the catalysts were obtained with an X-ray diffractometer (Bruker - D2 Phaser) operating with Cu Kα radiation (λ = 0.15406 nm) generated at 30 kV and 10 mA. The parameters were kept constant during the analysis: 2θ range = 20°–90°, and step = 0.025° s⁻¹. The catalysts composition phase was achieved by fitting the experimental angular range of interest to the pseudo-Voigt function per crystalline peak with the Profile Plus Executable refinement program (Siemens AG). Crystallite size was estimated from Debye-Scherrer equation, and the unit cell parameters were determined using the least-squares method by UFit. exe v1.3–1992 software. Energy-dispersive X-ray spectroscopy (EDX) was performed in a Leica Zeiss LEO 440 to check the homogeneity of the local elemental composition in each prepared material. Additionally, surface morphology was investigated with a high-resolution transmission electron microscopy (HRTEM) using a TECNAI G2F20 electron microscope in bright and dark field modes coupled with EDX analysis. X-ray photoelectron spectroscopy (XPS) was used to probe and characterize the surface and oxidation states. Analyses were performed on a Kratos Axis Ultra DLD spectrometer equipped with a monochromatic Al Kα X-ray source (1486.6 eV) operating at 15 kV and 10 mA (150 W). The analysis spot size is approximately 300 μm × 700 μm and the pass energy is 20 eV for recording high resolution spectra. The XPS data were calibrated by using the C1s (C–C) peak binding energy (B.E.) at 284.6 eV, and the spectra were fitted with CasaXPS software (version 2.3.17). Shirley background has been chosen and asymmetric Gaussian-Lorentzian profile functions were used to fit the spectra. The base pressure of the instrument was 9 × 10⁻⁸ Pa and the sample powder was pressed in a copper holder of 3 mm diameter and introduced into the preparation chamber after being outgassed overnight.

Electrochemical characterization of the electrode materials.—The electrochemical experiments were performed using an Autolab Potentiostat (PGSTAT302N, Metrohm). Cyclic voltammetry (CV) and Chronoamperometry (CA) measurements were carried out in a conventional three-electrode cell. The reference and counter electrodes were Hg/HgO/OH⁻ (0.1 mol l⁻¹ NaOH) and a vitreous carbon slab, respectively. In order to easily compare with recent literature, all the results are referred to the reversible hydrogen electrode (RHE) using Hg/HgO (E = -0.965 V vs RHE) conversion. The catalytic ink formulation was done 2.0 mg of the material

powder that was dispersed in a solution composed of 95 μl isopropanol and a 5 μl Nafion[®] suspension (5 wt.% in aliphatic alcohol Aldrich). Afterwards, the ink was homogenized in an ultrasound bath for 30 min. Finally, 3 μl of the ink was deposited uniformly onto a glassy carbon (GC) disk (3 mm diameter) previously polished with alumina and dried at room temperature. All the solutions were purged with N_2 for nearly 15 min before starting the electrochemical measurements. The CVs were recorded by potential cycling (0.05 to 1.15 V vs RHE) in a solution containing 0.10 mol l⁻¹ NaOH as electrolyte support and for the oxidation measurements we used a solution with 0.20 mol l⁻¹ glycerol at 10 mVs⁻¹ scan rate. The CA experiments were conducted at 0.55 V vs RHE for 30 min aiming to assess the catalyst stability, moreover, the composite effect on GEOR. The CO stripping measurements were carried out using an experimental protocol reported by Holade et al.⁴⁹ Briefly, CO was pre-adsorbed onto the catalyst surface a 0.1 V vs RHE by bubbling CO into 0.10 mol l⁻¹ NaOH for 300 s, followed by N_2 purge for 600 s to remove any residual free-CO from the solution. Finally, the CV curve was recorded in the potential range 0.10–1.2 V vs RHE at 10 mV s⁻¹ scan rate.

Analysis and identification of the reaction products by HPLC and FTIRS.—The Rh/SnO₂-C performance for glycerol conversion was investigated by electrolysis experiments carried out in potentiostatic conditions. The potential was fixed at 0.55 V vs RHE for 4 h using the programmed potential electrolysis (PPE) setup (Fig. S1 (available online at stacks.iop.org/JES/169/094502/mmedia)), which consisted of two potential steps: a first potential plateau was set at $E_{\text{ox}} = 0.55$ V vs RHE (60 s for electrooxidation of glycerol) and a second one fixed at $E_{\text{des}} = 1.4$ V vs RHE, for the regeneration of the catalytic surface or removal of the poison species. The reaction products were quantitatively determined by comparing their retention times with those of pure commercial standards injected under the same isocratic analysis conditions (external calibration). Aliquots were collected every 30 min and injected into high-performance liquid chromatography (HPLC, from Shimadzu, model LC-10AT) equipped with a double on-line detection system i.e., a UV-vis ($\lambda = 210$ nm) detector followed by a Refractive Index (RID-10A). The apparatus was also composed by an automatic injector with a 20 μl sample loop, and an ion exclusion column (Aminex HPX-87H, from BioRad). The mobile phase was a sulfuric acid solution (3.33 mmol l⁻¹ H₂SO₄) at a 0.6 ml min⁻¹ flow rate.

The SPAIRS (Single Potential Alteration Infrared Reflectance Spectroscopy) technique was used to monitor the presence of reaction intermediates and the formation of reaction products. The recorded spectral range is 1000–4000 cm⁻¹ and that of interest was herein between 1000 and 2500 cm⁻¹. The spectra were recorded with an 8 cm⁻¹ spectral resolution at 50 mV intervals between 0.1 and 1.2 V vs RHE at 1 mV s⁻¹ scan rate. The reflectance spectra were calculated for the different potential values as changes in the reflectivity (R_i) relative to a reference single-beam spectrum (R_0) as follows: $\Delta R/R = (R_i - R_0)/R_0$ as previously reported.⁶⁴ Electrochemical measurements, such as CO stripping, CV and CA experiments were coupled with the in situ FTIRS investigations. Thus, CO-stripping experiments in a 0.1 mol l⁻¹ NaOH solution were conducted using the same protocol described previously, by FTIRS data acquisition technique. Two SPAIRS methods were applied in this work: (i) the classical one consisted in acquiring spectra at 50 mV intervals at 1 mV s⁻¹ and in a potential domain; (ii) the second technique was coupling CA measurements to FTIRS

acquisition at fixed electrode potentials (0.55 and 0.70 V vs RHE) during 30 min. The working electrode used in this study was a vitreous carbon substrate (8 mm diameter) onto which the catalyst was deposited. The catalytic ink formulation was slightly modified to improve the reflectivity at the electrode/solution interface; so, isopropanol composition used was 375 instead of 95 μl , as described previously.

Cell voltage performance.—The DGFC driving force was evaluated using a home-made single acrylic two-compartment cell (Fig. S2) depicts the experimental setup). Firstly, the current-potential test was implemented with the Rh/SnO₂-C catalyst as anode (0.2 mg cm⁻² metal loading). The catalytic ink was prepared as described above, however, the volume of 17 μl was deposited onto both sides of a carbon Toray substrate (0.3 cm²). Palladium-iron (PdFe/C) 20 wt.% catalyst was used as cathode, considering its higher alcohol tolerance in case of fuel crossover in the cathodic compartment.⁶⁵ For an easy comparison of the results, the power density as function current density was evaluated for Rh/SnO₂-C, Pt/C and Pd/C catalysts as anodes. An Anion Exchange Membrane (AEM, Fumasep FAA, from Fumatech) pre-treated in a 1.0 mol l⁻¹ NaOH solution was used to physically separate the two compartments and to ensure the current relay between the electrodes. The fuel cell operated with a supporting electrolyte (0.5 mol l⁻¹ NaOH) at 25 °C in each compartment; there was an oxygen supply in the cathode and glycerol as fuel (0.1 mol l⁻¹) in the anodic side.

Results and Discussion

Physicochemical characterization.—The physicochemical characterization of the material samples was carried out to determine their crystallographic structure and elemental composition. Figure 1a depicts the SnO₂-C, Rh/C, and Rh/SnO₂-C XRD patterns collected between 20 and 90°. The first peak assigned in Rh/C sample at $2\theta = 25^\circ$ is the carbon Vulcan (002) reflection plane. The materials' crystallinity was confirmed by the well-defined peaks. Firstly, evaluating the SnO₂-C composite it was found that the observed diffraction pattern corresponded to SnO₂ crystallographic structure, with peaks at $2\theta = 26.5, 33.9, 38.0, 51.8, 64.8,$ and 78.72° assigned to the (110), (101), (200), (211), (112), and (321) planes, respectively, according to standard JCPDS values (JCPDS No. 01-088-0287).⁶⁶ The absence of the carbon peak or rather its attenuation for both compositions containing SnO₂-C could be related to the amorphous nature of carbon. Additionally, no peaks assigned to SnO or metallic Sn are detected indicating the material phase purity, which highlights the efficiency of the preparation method of SnO₂-C composite. The main peak in the XRD pattern of Rh/C is observed at 41.03 and corresponds to (111) facet of Rh face-centered cubic (*fcc*) structure. In the Rh/SnO₂-C catalyst diffraction pattern, this peak is negatively shifted to 39.53° suggesting the alloy formation between Sn and Rh during the synthesis process. As described previously,^{54,67} the Rh mean crystallite sizes were estimated with the Rh (111) peak according to Debye-Scherrer's equation and are summarized in Table I. The obtained values were of *ca.* 1.8 and 2.0 nm, for Rh/SnO₂-C and Rh/C, respectively, which indicate a nanometric scale in the prepared materials. As a comparison, Nishida et al.⁶⁸ prepared Rh/C by microwave-assisted alcohol reduction method and the Rh crystallites were of *ca.* 9.5 nm size. Therefore, the synthetic polyol approach proposed herein is a straightforward method for obtaining small crystallite sizes.

Table I. Physicochemical parameters determined by XRD measurements for Rh/C, Rh/SnO₂-C, catalysts.

Electrocatalyst	2θ (degrees)	Crystallite size (nm)	Lattice parameter (nm)	Alloying degree (%)
Rh/C	40.82	2.0	0.3825	—
Rh/SnO ₂ -C	38.93	1.8	0.4003	63

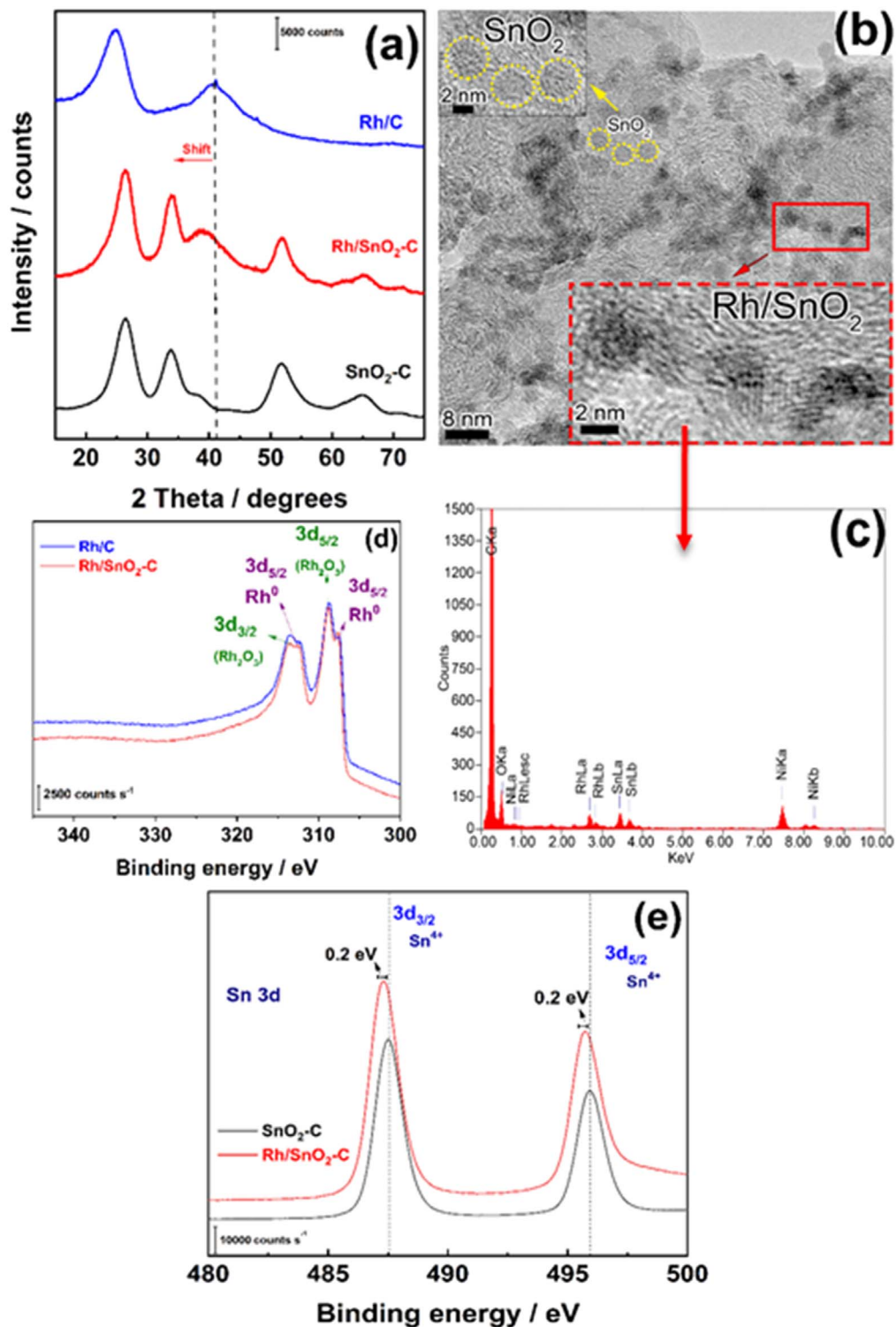


Figure 1. (a) XRD diffraction patterns of the Rh/C, SnO₂-C, and Rh/SnO₂-C catalysts; (b) TEM images of SnO₂-C and Rh/SnO₂-C catalyst; (c) EDX spectra recorded on the isolated Rh/SnO₂-C nanoparticles; (d) Rh 3d spectra level of Rh/C and Rh/SnO₂-C prepared catalysts; (e) Sn 3d spectra level of Rh/SnO₂-C and SnO₂-C prepared catalysts.

The lattice parameter (a_{hkl}), calculated from the Rh (111) diffraction peak positions in XRD patterns,⁶⁹ is also shown in Table I. The Rh/C sample experimental lattice parameter was 0.3825 nm, which is similar to the theoretical value (0.3820 nm).⁷⁰ On the other hand, for Rh/SnO₂-C an expansion effect in the lattice parameter (0.4003 nm) was observed, in agreement with previously reported studies for Rh–Sn alloy nanoparticles.⁷¹ As explained by Kou et al.⁷² this could be ascribed by the difference between the

radii of Rh (1.35 Å) and Sn (1.45 Å). The latter being higher, the lattice parameter is increased by the substitution of Rh by Sn, confirming the formation of alloy. The alloying degree calculated for Rh/SnO₂-C sample using Vegard's law⁷³ was found to reach the high value of about 63%, which, as reported, would result in enhanced catalytic activity and stability.^{46,74,75}

Figure 1b shows representative TEM images obtained on SnO₂-C and Rh/SnO₂-C materials. As can be seen, SnO₂ nanoparticles are

well dispersed on the carbon support for SnO₂-C (Fig. 1b). Then, it is observed in Rh/SnO₂-C that Rh nanoparticles are evenly dispersed on the SnO₂-C composite support with few agglomerations. Moreover, the Rh nanoparticles were small and do not present a defined and even morphology, although they are mostly spherical. Additionally, it was noted a different color intensity in the regions where Rh is deposited as compared to regions with only SnO₂ nanoparticles. Therefore, the main interest of this synthesis approach is also related to the Rh deposition. Indeed, it is very important to know whether the Rh deposition occurs over the SnO₂ or C particles in the composite support in order to understand the role of the support in the catalytic activity. EDX analyses were performed and Fig. 1c shows the spectra recorded on isolated particles revealing the presence of the two metals in the nanoparticles confirming the deposition of Rh onto SnO₂ and also in agreement with Rh-Sn alloy formation. To get additional evidence on alloy formation, XPS analyses were also carried out. The Rh 3d XPS spectra obtained for Rh/C and Rh/SnO₂-C catalysts are shown in Fig. 1d, while Sn 3d XPS spectra of SnO₂-C and Rh/SnO₂-C are depicted in Fig. 1e. For the Rh 3d region, metallic (Rh⁰) and oxidized Rh₂O₃ (Rh⁺³) phases are indicated. For both catalysts, the 3d_{5/2} transition peaks assigned to Rh⁰ and Rh⁺³ were observed at 307.2 and 308.3 eV (Fig. 1d), respectively, and the corresponding 3d_{3/2} transitions were observed at 311.8 and 313.1 eV. For the Sn 3d region, two peaks are observed and assigned to 3d_{3/2} and 3d_{5/2} transitions. A shift of 0.2 eV was observed between the peaks of SnO₂-C and those of Rh/SnO₂-C. According to Korotcenkov et al.⁷⁶ this electronic effect could indicate the formation of Rh-Sn alloy.

Electrochemical characterization.—Electrochemical characterization of Rh/C and Rh/SnO₂-C was performed in N₂-saturated 0.1 mol l⁻¹ NaOH at 10 mV s⁻¹. Figure 2a shows the CVs

normalized with the Rh charge loading deposited onto the glassy carbon support. Both CV curves exhibit a typical supported Rh profile in alkaline medium.⁷⁷ However, it is easily observed the carbon-support influence on the CV area, which increases with Rh/SnO₂-C as compared to Rh/C, indicating that the former presents a larger electrochemically active surface area in line with the previous Soares et al.³⁰ study. When also regarding the positive ongoing scan, the hydrogen adsorption/desorption region is also increased with Rh/SnO₂-C and the hydroxide/oxide oxidation region becomes larger with plausible co-oxidation of Sn surface. Furthermore, during the negative scan the Rh oxide reduction process is shifted to positive potential values (0.40 V vs RHE) on Rh/SnO₂-C, indicating that the oxide composite support weakens the OH⁻ adsorption.⁷⁸ Consequently, it increases the active sites reducing the coulombic charge necessary to reduce the Rh oxide species.

Carbon monoxide (CO) was widely reported as one of the main poisoning intermediates that damaged the electrode active sites during the alcohol oxidation reaction in fuel cell systems, especially anodes.^{79–83} Thereby, in the objective to develop these materials for DGFC applications, it is crucial to evaluate CO tolerance ability on the catalyst surface. Figure 2b shows the linear polarization curves in 0.10 mol l⁻¹ NaOH and at 10 mV s⁻¹ during the CO stripping experiments. Initially, on the Rh/SnO₂-C electrode, the curve shape changes compared with Rh/C, suggesting a high CO oxidation efficiency. Moreover, it is observed that the CO oxidation peak on Rh/SnO₂-C exhibits a negative energy shift (~60 mV), indicating that the SnO₂ may facilitate the catalytic activity by removing the adsorbed CO from the Rh surface. Two different effects may explain this sudden improvement on CO-poisoning in Rh-SnO₂/C; (i) the bifunctional mechanism^{71,84–86} and (ii) the ligand effect due to electronic properties changes in the catalytic center.^{87–91} Therefore,

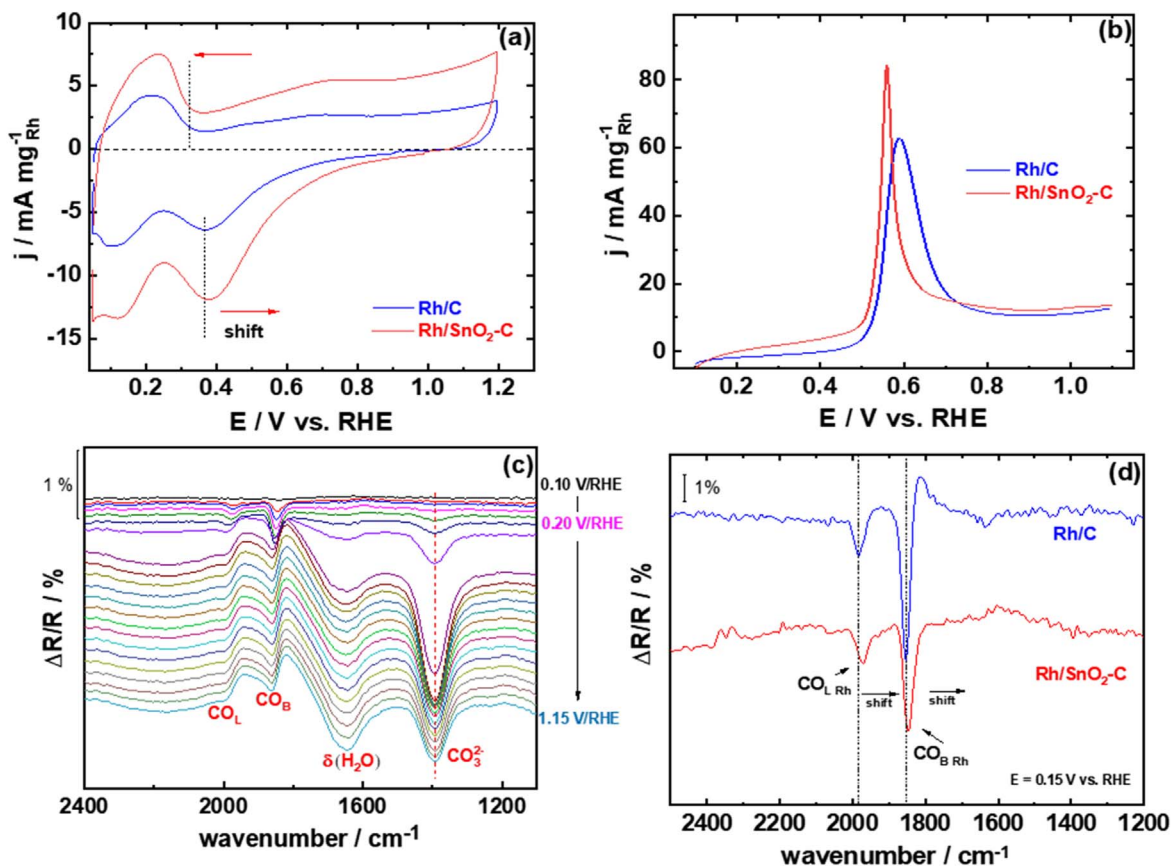


Figure 2. (a) CVs of the Rh/C and Rh/SnO₂-C electrodes recorded in 0.10 mol l⁻¹ NaOH at room temperature and at 10 mV s⁻¹; (b) CO stripping on Rh/C and Rh/SnO₂-C electrodes recorded in a 0.1 mol l⁻¹ NaOH solution at 10 mV s⁻¹; (c) SPAIR spectra of the species from CO oxidation in 0.1 mol l⁻¹ NaOH on Rh/SnO₂-C. Reference spectrum taken at 0.10 V vs RHE; (d) FTIR spectra obtained during the CO stripping at 0.15 V vs RHE on Rh/C and Rh/SnO₂-C.

to verify more carefully the main effect on Rh/SnO₂-C sites during CO oxidation reaction, CO stripping experiments coupled with in situ FTIR spectroscopy were conducted.

Figure 2c depicts a series of spectra acquired during CO stripping at 1 mV s⁻¹ on Rh/SnO₂-C, taking the spectrum obtained at 0.10 V vs RHE as a reference. The main bands at 1987 and 1856 cm⁻¹ observed at the beginning are assigned, respectively, to linearly adsorbed (CO_L) and bridge bonded (CO_B) CO on Rh.^{92,93} According to previous studies,⁹⁴ CO molecules do not adsorb on Sn and therefore no band is expected for CO adsorbed on Sn. Then, the bands at 1392 and 1610 cm⁻¹ were assigned to the symmetric (ν_s (COO)) vibration of carbonate (CO₃²⁻) ions and the water O-H bending, respectively.⁹⁵ The alloy formation effect, revealed by XRD and XPS results, is herein highlighted by the modification on the onset potential for carbonate formation, which starts at 0.20 V vs RHE on Rh/SnO₂-C, while on Rh/C this onset takes place at 0.40 V vs RHE (Fig. S3). These results emphasize the Rh/SnO₂-C ability of CO₃²⁻ formation at lower potentials. So, regarding the effect between the catalytic sites and probe chemisorbed molecules, previous studies demonstrated that CO adsorbed band's intensity as a function of the applied potential brings to light relevant information on how the vibration frequency strongly depends on the electronic properties of the adsorption site.^{92,96} However, in some studies, it was not easy to establish these direct relations between the applied potential and CO adsorbed bands' intensity due to the Stark effect,⁹⁷ which can affect the band intensity during the reaction therefore shifting the CO bands to lower or higher wavenumbers. This effect was previously reported for Rh catalysts wherein the C-O stretching frequency exhibits a typical Stark shift with a slope reaching 34 cm⁻¹ V⁻¹.^{92,93} Therefore, to minimize the Stark effect, Fig. 2d depicts the CO adsorption bands frequency spectra on the Rh/C and Rh/SnO₂-C at 0.15 V vs RHE; this potential was chosen to avoid CO oxidation, which starts at 0.20 V vs RHE. A decrease in the wavenumber of both CO_L and CO_B bands is observed for Rh/SnO₂-C catalyst as compared to Rh/C, though the shift becoming more pronounced on CO_L. These shifts can be interpreted in terms of electron-donating properties of the oxide composite support, where the SnO₂ increases near Rh and reduces the Rh-CO_{Ads} bond strength by donor effect. SnO₂ acts therefore as an electron density donor to Rh and this effect is responsible for the CO oxidation at lower potential.⁹⁸⁻¹⁰⁰

Glycerol oxidation reaction on Rh/C and Rh/SnO₂-C catalysts.—Figure 3a depicts the CVs profiles for 0.2 mol l⁻¹ glycerol oxidation in alkaline medium at 10 mV s⁻¹ on Rh/C and Rh/SnO₂-C. The CVs were normalized with respect to the Rh amount deposited onto the conductive support. As can be noticed, Rh/SnO₂-C shows a

much higher current density towards glycerol oxidation than Rh/C. Indeed at 0.63 V vs RHE, the current density on the metal oxide composite is almost 4.5-fold that of Rh/C. Moreover, the onset potential is also affected, and the GEOR starts almost 100 mV earlier on Rh/SnO₂-C, evidencing that the Rh interaction with the composite support improving the donor effect results in a glycerol oxidation kinetics enhancement.¹⁹

The stability is also a key parameter when developing anode catalysts for DGFC's devices. Therefore, the electrochemical Rh/SnO₂-C durability was investigated herein by using chronoamperometry. Although this measurement is not like the polarization curve of an electrode material operating in a fuel cell, these results still provide an insight of the reaction kinetics at a given potential. Figure 3b shows the Rh/C and Rh/SnO₂-C chronoamperometric curves at 0.55 V vs RHE. The Rh/SnO₂-C catalyst exhibits much higher current density values than Rh/C over the entire time range. These results stress the metal oxide composite catalyst ability to decrease the poisoning effect due to intermediates compounds of the incomplete GEOR, and thereby to increase the electrode stability. This trend was also discussed in other studies using SnO₂-C carbon oxide composite as a support in EOR and methanol oxidation reaction (MOR)^{30,43} due to the Sn ability to bond with OH molecules and the electronic effect (as demonstrated in Fig. 2d) between the metal and the oxide composite.^{71,85,87}

Concerning DGFC device applications, the main goal is the development of anode materials that provide high current densities at low potentials.¹⁰¹ Consequently, during the electrolysis measurements it is crucial to evaluate that the chosen potential value meets both features. Thereupon, chromatographic analyses were performed on the recovered electrolyte when CA measurements were realized at 0.55 V vs RHE on Rh/SnO₂-C, an applied potential value significantly lower compared to reported studies. For example, Lima et al.¹⁰² performed HPLC analyses of the GEOR products on Ag/C and PtAg/C catalysts at 0.8 V vs RHE in alkaline medium, which is 250 mV higher than the potential applied herein and undoubtedly demonstrates the benefit of using Rh/SnO₂-C for GEOR. Thus, Table II shows the quantitative glycerol conversion results at 0.55 V vs RHE for Rh-SnO₂/C, which reached 30% of glycerol consumption after 4 h of electrolysis. This result can be considered attractive for the electrochemical glycerol conversion, mainly due to the ability of the catalyst to perform at low potential values. For comparison, Holade et al.¹⁰³ demonstrated that glycerol conversion on PdAg/C reached 24% after 4 h at 0.8 V vs RHE, a potential higher than that set herein.

Table II also displays the selectivity and the faradaic yields of the reaction products determined during electrolysis. Glycerate, the main product, is selectively produced at 28.4%; tartronate (7.9%),

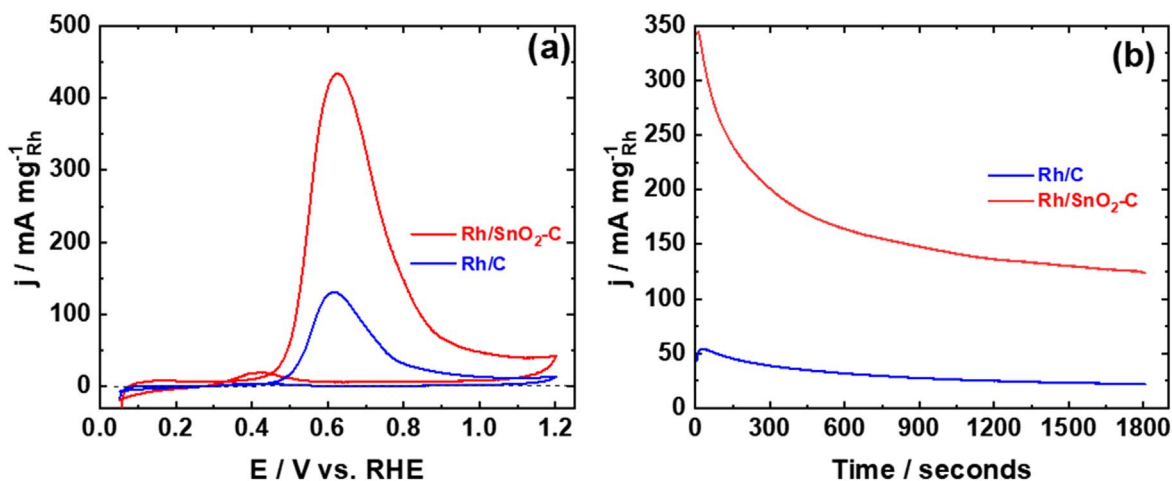


Figure 3. (a) CVs of Rh/C and Rh/SnO₂-C recorded in 0.10 mol l⁻¹ NaOH in the presence of 0.2 mol l⁻¹ glycerol at 10 mVs⁻¹; (b) Chronoamperometry curves for GEOR at 0.55 V vs RHE during 1800 s in 0.10 mol l⁻¹ NaOH and the presence of 0.2 mol l⁻¹ glycerol.

Table II. Distribution of the reaction production resulted from the electrocatalytic oxidation of 0.2 M glycerol on Rh/SnO₂-C, at 0.55 V RHE in 0.1 M NaOH.

Glycerol conversion after 4 h long-term electrolysis	Selectivity of the reaction product ^{a)}					Faradaic yield of the reaction product ^{b)}				
	Glycerate	Tartronate	Glycolate	Oxalate	Formate	Glycerate	Tartronate	Glycolate	Oxalate	Formate
30.3%	0.43 mmole 28.4%	0.12 mmole 7.9%	0.13 mmole 5.7%	0.14 mmole 6.1	0.17 mmole 3.7%	34.0%	19.1%	12.9%	20.2%	8.9%

a) Selectivity ($S_i = \frac{1}{\nu_i} \times \frac{C_{i,t}}{C_0 - C_t} \times 100$), where ν_i is the stoichiometric coefficient of the reaction product. b) Faradaic yield $FE_i = \frac{nFVC_{i,t}}{\int I(t) dt}$, where $\int I(t) \times dt$ represents the integration of Fig. S1b ($Q_{\text{exp}} = 488$ C).

glycolate (5.7%), oxalate (6.1%), and formate (3.7%) were also determined by external calibration from the chromatographic analysis of the electrolytic solution after 4 h. Moreover, the Rh/SnO₂-C ability to break the C–C bonds at low potentials was confirmed by oxalate, glycolate, and formate production during the glycerol oxidation, which involves lots of electrons and a large part of electrical charge. The distribution of the reaction products from the chromatographic analysis and related to the glycerol consumption during the 4 h electrolysis is 0.058 mol l⁻¹ e.g, a mass balance close to 96%. If one considers the results obtained by FTIRS (Figs. 4a and 4b) and the 488C quantity of electricity generated during the electrolysis (Figs. S1b and S1c), the missing mass could mainly be attributed to the formation of CO₃²⁻^{102,103} (Table II).

In order to get further insights on the GEOR mechanism on Rh/SnO₂-C at low potentials, FTIRS experiments were coupled with chronoamperometry measurements. Figure 4a shows the accumulated FTIR spectra obtained at 0.55 V vs RHE during 1800 s. In accordance with HPLC results, the same functional groups (carboxyl, hydroxyl...) were identified by comparing them with standards recorded in the same electrolytic medium (Figs. S4 and S5). Therefore, as suggested by HPLC measurements, the C–C cleavage was confirmed by the band at 1838 cm⁻¹ corresponding to the CO_B adsorbed formation.¹⁰⁴ The other main bands were assigned as follows: 1581 cm⁻¹ (tartronate), 1389 cm⁻¹ (CO₃²⁻), 1108 cm⁻¹ (glycerate), 1074 cm⁻¹ (glycolate), and 1220 cm⁻¹ (glyceraldehyde).^{103–106} The FTIRS aldehyde evidence is important because, as mentioned above, its HPLC determination is complicated due to the nucleophilic attack on the carbonyl function resulting in glycerate. Similarly, the RID low sensitivity can make the CO₃²⁻ quantification difficult, however, it was demonstrated by Lima's group¹⁰² that it is possible to confirm the high CO₃²⁻ concentration due to difference in the relative intensity band between carbonyl containing compounds (at 1581 cm⁻¹) and CO₃²⁻ (at 1389 cm⁻¹). Therefore, as it can easily be observed, the intensity of the CO₃²⁻ band (at 1581 cm⁻¹) is largely higher than that of carboxylate compounds (at 1581 cm⁻¹) indicating therefore the very high quantity of carbonate formed at 0.55 V vs RHE. This may suggest that Rh/SnO₂-C favors the C1 formation at 0.55 V vs RHE by C–C cleavage as previously noticed by Garcia et al.¹⁰⁷ for PtAg catalyst supported on manganese oxide-carbon composite. At this stage, two explanations can be put forward to explain the beneficial effect in the activity and selectivity of Rh/SnO₂-C: (i) the electronic effect due to the Rh–Sn alloy formation¹⁰⁸ (Fig. 1b), which weakens the intermediates adsorption strength formed during the oxidation reaction; (ii) the SnO₂-C acts as a source of oxygenated groups (OH_{ads}) by bifunctional mechanism and following a Langmuir–Hinshelwood (LSH) mechanism.^{71,84–86}

At last, the band observed at 2343 cm⁻¹ corresponding to CO₂ antisymmetrical vibration was also previously reported by some authors^{103,105} and indicates the pH change of the thin observed layer nearby the electrode during the reaction. Indeed, the decrease in OH⁻ concentration due to its consumption by the reaction and diffusional limitations coming from the experimental constraints result in local pH, a low pH nearby the electrode, and this even in alkaline medium, and thereby CO₂ is formed and observed before diffusing to the bulk solution where it is converted into carbonate.

Figure 4b depicts the FTIR spectra obtained at 0.70 V vs RHE, where the main change was noticed in the bands centered at around 1400 cm⁻¹. Two distinct bands centered at 1310 and 1358 cm⁻¹ corresponding to oxalate, and formate ions, respectively, are clearly observed. At the same time the carbonate band becomes almost negligible. This result clearly indicates, on the one hand, that the increase in electrode potential emphasizes the formation of C2 and C1 products; on the other hand, and unlike the findings of Hiltrop et al.¹⁰⁹ on Pd/CNT in 1 M NaOH, the accumulation of C1 products is not converted herein, on Rh/SnO₂-C, to more carbonate concentration which decreases at high potentials.

Finally, it is well stated that the GEOR on the Pt-based and Pd-catalysts usually follows two pathways involving glyceraldehyde

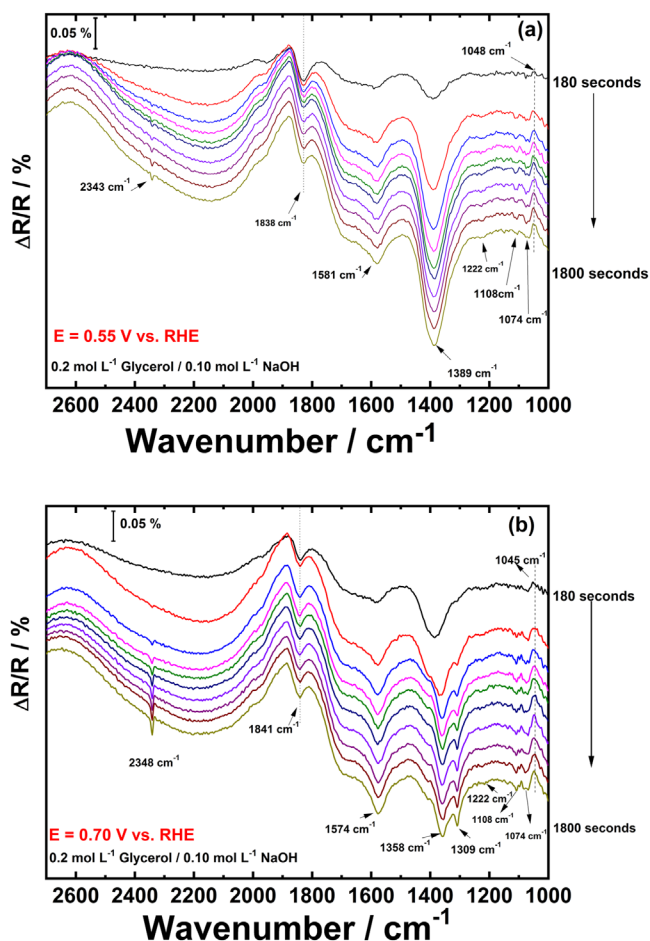


Figure 4. (a) FTIR spectra recorded during chronoamperometry experiment on Rh/SnO₂-C catalyst at 0.55 V vs RHE; (b) FTIR spectra recorded during chronoamperometry experiment on Rh/SnO₂-C catalyst at 0.70 V vs RHE in a 0.10 mol l⁻¹ NaOH electrolytic solution.

and/or dihydroxyacetone.^{110–112} The HPLC combined with FTIRS results suggested that on Rh/SnO₂-C the route in the alkaline medium involving glyceraldehyde is the most probable. Based on the obtained results, a glycerol electrooxidation reaction scheme over Rh/SnO₂-C is assumed and illustrated in Fig. 5. Firstly, during the beginning of GEOR, glycerol is converted to glyceraldehyde, chemically unstable in NaOH media (HO⁻ nucleophilic attack of –CHO to –COO⁻),¹¹³ and subsequently oxidized to glycerate ion. Eventually, the glycerate was rapidly oxidized to tartronate and/or glycolate, the latter involving C–C cleavage. But, as demonstrated by Liu et al.¹⁷ and herein confirmed by HPLC quantification, the glycerate conversion also results in the formate and, subsequently, carbonate production. Holade et al.¹⁰³ also demonstrated that at this stage, the formate formation also results in adsorbed CO and therefore carbonate. Furthermore, carbonate is also formed when glycolate is oxidized to oxalate and, finally, into carbonate. As discussed above, when increased the potential value, the C–C cleavage decreases, promoting most of formate and oxalate, while at lower potential values the formation of carbonate is favored.

DGFC testing in a home-made cell at room temperature.—To evaluate the promising characteristics of the as-prepared Rh/SnO₂-C catalyst, the DGFC testings were conducted in a home-made acrylic cell (Fig. S2), which was composed of two compartments separated with an anion exchange membrane.¹¹⁴ Firstly, it is essential to emphasize that this investigation was mainly focused on each component's behavior during the GEOR, aiming to perform an analysis of the electrolytic solution by liquid chromatography.

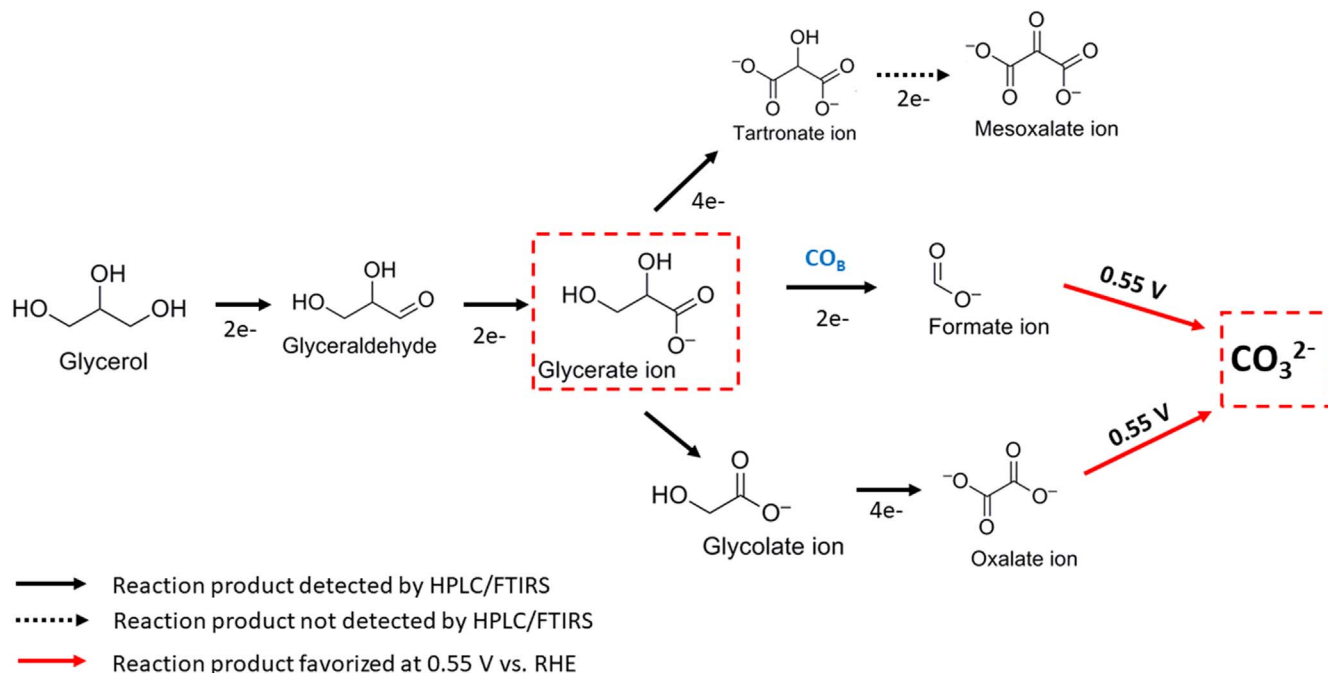


Figure 5. Reaction pathway scheme for GEOR on the Rh/SnO₂-C catalyst in alkaline medium (0.1 mol l⁻¹ NaOH).

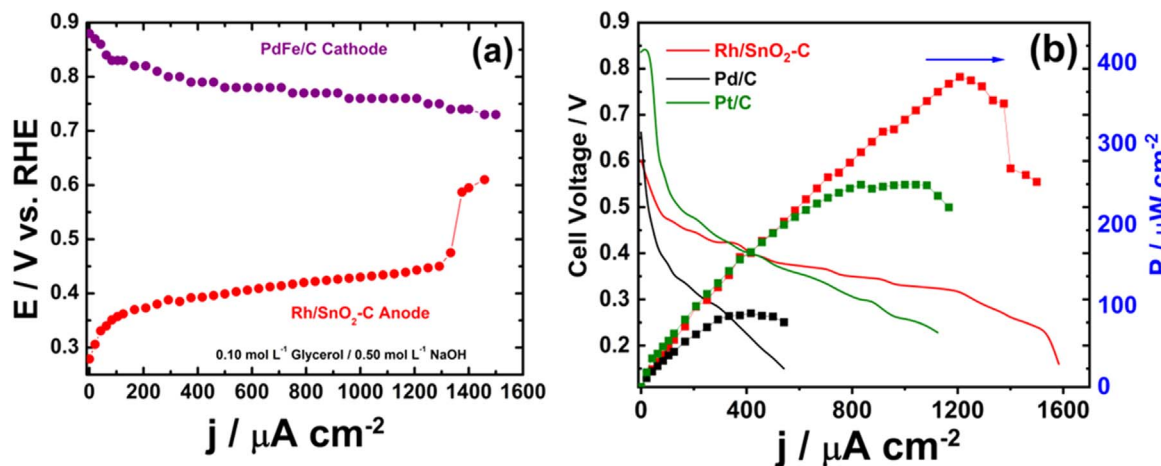


Figure 6. (a) E-j polarization curves obtained at the electrodes of a DGFC operating at room temperature and in alkaline medium where: Rh/SnO₂-C anode fed with 0.1 mol l⁻¹ glycerol and 0.5 mol l⁻¹ NaOH; PdFe/C cathode fed with O₂; (b) Electrochemical performance of a DGFC at 25 °C using PdFe/C (0.2 mg cm⁻²) as cathode catalyst; the anodic compartment contains 0.5 mol l⁻¹ NaOH and 0.1 mol l⁻¹ glycerol separated to the cathodic one with a Fumatech membrane.

Consequently, the electrode materials were not coated on the membrane as membrane electrode assembly (MEA) (as can be observed in Fig. S2). Therefore, the polarization curves were carried out at room temperature and using a PdFe/C as a cathode (Figs S6-S8). This choice was based on the recently reported performance in the ORR and the high tolerance to alcohol and CO species^{49,115,116} of this material. Figure 6a shows the polarization curves of Rh/SnO₂-C and PdFe/C as anode and cathode, respectively. A reference electrode (Hg/HgO/OH⁻ (0.1 mol l⁻¹)) was included in each compartment, and the polarization curves were recorded separately. The ORR starts at 0.90 V vs RHE and the potential decreases slightly during the working interval. The anode profile shows an increase in the potential from 0.25 vs RHE and then, a decrease of up to 1300 μA cm⁻² was observed. This behavior demonstrated that the anode was the electrode that limits the GEOR reaction in this cell configuration. Nevertheless, Fig. 6b shows the output power density of 390 μW cm⁻² compared to

97 μW cm⁻² on the Pd/C, and 249 μW cm⁻² on Pt/C catalyst (both prepared by the same polyol method). As can be observed, the Rh/SnO₂-C electrocatalyst presents the superior electrochemical performance with the largest current densities in the whole studied range. The power density was found to be 3.9-fold higher on Rh/SnO₂-C than on the Pd/C anode. Thus, it is possible to confirm that the GEOR is proceeding more rapidly on the Rh/SnO₂-C surface. The promoting effect due to the alloy formation and the increased oxygenated groups' presence are once again highlighted.

Conclusions

Rh/C and Rh/SnO₂-C catalysts were successfully prepared by polyol method and used to evaluate the GEOR in alkaline medium. The nanoparticles showed a distribution size of 2.0 and 1.8 nm in Rh/C and Rh/SnO₂-C, respectively. Electrochemical measurements were coupled with spectroelectrochemistry (FTIRS) and the results

were correlated to physicochemical characterizations for understanding the electronic effect between Rh and Sn during the synthesis process. Additionally, the HPLC and the FTIRS results provided evidence of formation of glycerate and then CO_3^{2-} as the main GEOR products at 0.55 V vs RHE. The coupling of FTIRS and CA measurements allowed to reveal the carbonate formation highlighted as the C–C–C bond cleavage ability of the Rh/SnO₂-C catalyst surface. The results indicated that on Rh/SnO₂-C catalysts the reaction follows the glyceraldehyde pathway. The strong interaction between Rh and the SnO₂-C composite directs the oxidation reaction of glycerol via the glycerate formation which then undergoes a C–C–C bond cleavage at low potentials, which is not emphasized on Rh deposited on carbon alone. Rh/SnO₂-C consisting of an alloying degree more than 63%, is a promising anode catalyst in DGFC application since it allows a better glycerol conversion and enhances the power density, i.e. 4-fold higher than those obtained on Pd/C and Pt/C under the same operating conditions. The physicochemical properties of the anode such as the high alloying degree may explain the beneficial ensemble (electronic and bifunctional) effects on the GEOR.

Acknowledgments

The authors thank CAPES and CNPq for financial support. “This study was financed in part by the Coordenação de Aperfeiçoamento de Pessoal de Nível Superior - Brasil (CAPES) - Finance Code 001.” The collaborative program CAPES/COFECUB under grant n° 914/18 are gratefully acknowledged. The authors also acknowledge the European Union (ERDF), “Région Nouvelle-Aquitaine” and EDF (M-2021-2) for their financial supports.

Notes

The authors declare that they have no known competing financial interests or personal relationships that could have appeared to influence the work reported in this paper.

ORCID

Thamyres F. M. Moreira  <https://orcid.org/0000-0001-7326-8022>
 K. Boniface Kokoh  <https://orcid.org/0000-0002-5379-7792>
 Teko W. Napporn  <https://orcid.org/0000000315067139>
 Paulo Olivi  <https://orcid.org/0000-0001-8614-8417>
 Cláudia Morais  <https://orcid.org/0000-0003-0096-2122>

References

- M. A. F. Akhairi and S. K. Kamarudin, *Int. J. Hydrogen Energy*, **41**, 4214 (2016).
- D. M. Fadzillah, S. K. Kamarudin, M. A. Zainoodin, and M. S. Masdar, *Int. J. Hydrogen Energy*, **44**, 3031 (2019).
- H. S. Ferreira, M. Gocyla, H. S. Ferreira, R. G. O. Araujo, C. V. S. Almeida, M. Heggen, R. E. Dunin-Borkowski, K. I. B. Eguiluz, P. Strasser, and G. R. Salazar-Banda, *J. Nanosci. Nanotechnol.*, **20**, 6274 (2020).
- R. M. Castagna, J. M. Sieben, A. E. Alvarez, and M. M. E. Duarte, *Int. J. Hydrogen Energy*, **44**, 5970 (2019).
- S. A. N. M. Rahim, C. S. Lee, F. Abnisa, M. K. Aroua, W. A. W. Daud, P. Cognet, and Y. Pérès, *Sci. Total Environ.*, **705**, 135137 (2020).
- E. Antolini, *Catalysts*, **9**, 980 (2019).
- M. S. Ahmad, C. K. Cheng, R. Kumar, S. Singh, K. A. Saeed, H. R. Ong, H. Abdullah, and M. R. Khan, *Electroanalysis*, **32**, 1139 (2020).
- M. S. E. Houache, K. Hughes, and E. A. Baranova, *Sustain. Energy Fuels*, **3**, 1892 (2019).
- I. Iliuta and M. C. Iliuta, *Int. J. Hydrogen Energy*, **45**, 18574 (2020).
- A. Cornejo, I. Barrio, M. Campoy, J. Lázaro, and B. Navarrete, *Renew. Sustain. Energy Rev.*, **79**, 1400 (2017).
- G. D. Yadav and P. A. Chandan, *Catal. Today*, **237**, 47 (2014).
- P. A. Alaba, C. S. Lee, F. Abnisa, M. K. Aroua, P. Cognet, Y. Pérès, and W. M. A. W. Daud, *Rev. Chem. Eng.*, **37**, 779 (2021).
- C. Coutanceau, S. Baranton, and R. S. B. Kouamé, *Front. Chem.*, **7**, 100 (2019).
- R. G. Da Silva, S. Aquino Neto, K. B. Kokoh, and A. R. De Andrade, *J. Power Sources*, **351**, 174 (2017).
- K. Zakaria, M. McKay, R. Thimmappa, M. Hasan, M. Mamlouk, and K. Scott, *ChemElectroChem*, **6**, 2578 (2019).
- N. Yahya, S. K. Kamarudin, N. A. Karim, M. S. Masdar, K. S. Loh, and K. L. Lim, *Energy Convers. Manag.*, **188**, 120 (2019).
- C. Liu, M. Hirohara, T. Maekawa, R. Chang, T. Hayashi, and C.-Y. Chiang, *Appl. Catal. B: Environ.*, **265**, 118543 (2020).
- Y. Kwon, Y. Birdja, I. Spanos, P. Rodriguez, and M. T. M. Koper, *ACS Catal.*, **2**, 759 (2012).
- P. Sangkheaw, S. Therdthianwong, A. Therdthianwong, N. Wongyao, and S. Yongprapat, *Renew Energy*, **161**, 395 (2020).
- E. Ferreira Frota, V. V. Silva de Barros, B. R. S. de Araújo, Â. Gonzaga Purgatto, and J. J. Linares, *Int. J. Hydrogen Energy*, **42**, 23095 (2017).
- H. Du, K. Wang, P. Tsiakaras, and P. K. Shen, *Appl. Catal. B: Environ.*, **258**, 117951 (2019).
- C. R. Zanata, C. A. Martins, É. Teixeira-Neto, M. J. Giz, and G. A. Camara, *J. Catal.*, **377**, 358 (2019).
- A. Nakova, M. Ilieva, T. Bojadjieva-Scherzer, and V. Tsakova, *Electrochim. Acta*, **306**, 643 (2019).
- D. Lee, Y. Kim, Y. Kwon, J. Lee, T.-W. Kim, Y. Noh, W. B. Kim, M. H. Seo, K. Kim, and H. J. Kim, *Appl. Catal. B: Environ.*, **245**, 555 (2019).
- F. Yang, J. Ye, Q. Yuan, X. Yang, Z. Xie, F. Zhao, Z. Zhou, L. Gu, and X. Wang, *Adv. Funct. Mater.*, **30**, 1908235 (2020).
- M. S. Ahmad, S. Singh, C. K. Cheng, H. R. Ong, H. Abdullah, M. R. Khan, and S. Wongsakulphasatch, *Catal. Commun.*, **139**, 105964 (2020).
- N. Li, W.-Y. Xia, C.-W. Xu, and S. Chen, *J. Energy Inst.*, **90**, 725 (2017).
- M. S. E. Houache, E. Cossar, S. Ntais, and E. A. Baranova, *J. Power Sources*, **375**, 310 (2018).
- Z. Zhang, L. Xin, and W. Li, *Int. J. Hydrogen Energy*, **37**, 9393 (2012).
- L. A. Soares, C. Morais, T. W. Napporn, K. B. Kokoh, and P. Olivi, *J. Power Sources*, **315**, 47 (2016).
- P. Mukherjee, P. S. Roy, and S. K. Bhattacharya, *Int. J. Hydrogen Energy*, **40**, 13357 (2015).
- M. Li, W. P. Zhou, N. S. Marinkovic, K. Sasaki, and R. R. Adzic, *Electrochim. Acta*, **104**, 454 (2013).
- K. Bergamaski, E. R. Gonzalez, and F. C. Nart, *Electrochim. Acta*, **53**, 4396 (2008).
- B. T. X. Lam, M. Chiku, E. Higuchi, and H. Inoue, *Adv. Nanopart.*, **5**, 60 (2016).
- Y. Kang, Q. Xue, P. Jin, J. Jiang, J. Zeng, and Y. Chen, *ACS Sustain. Chem. Eng.*, **5**, 10156 (2017).
- G. M. Alvarenga and H. M. Villullas, *Curr Opin Electrochem*, **4**, 39 (2017).
- S. Hussain et al., *Electrochim. Acta*, **316**, 162 (2019).
- S. C. Zignani, V. Baglio, D. Sebastián, S. Siracusano, and A. S. Aricò, *Electrochim. Acta*, **191**, 183 (2016).
- Z. Li, C. Kong, and G. Lu, *Int. J. Hydrogen Energy*, **40**, 9061 (2015).
- J. C. Matsubu, S. Zhang, L. DeRita, N. S. Marinkovic, J. G. Chen, G. W. Graham, X. Pan, and P. Christopher, *Nat. Chem.*, **9**, 120 (2017).
- E. Priyadarshini, S. Suresh, S. Srinivasan, and A. Manikandan, *Physica B*, **566**, 17 (2019).
- W.-H. Qu, F. Han, A.-H. Lu, C. Xing, M. Qiao, and W.-C. Li, *J. Mater. Chem. A*, **2**, 6549 (2014).
- B. Ruiz-Camacho, H. H. R. Santoyo, J. M. Medina-Flores, and O. Álvarez-Martínez, *Electrochim. Acta*, **120**, 344 (2014).
- X. Fan, J. Shao, X. Xiao, X. Wang, S. Li, H. Ge, L. Chen, and C. Wang, *J. Mater. Chem. A*, **2**, 18367 (2014).
- F. Zhu, K. Tu, L. Huang, X. Qu, J. Zhang, H. Liao, Z. Zhou, Y. Jiang, and S. Sun, *Electrochim. Acta*, **292**, 208 (2018).
- C. Zhu, S. Guo, and S. Dong, *Adv. Mater.*, **24**, 2326 (2012).
- B. Li, W. Su, X. Wang, and X. Wang, *Int. J. Hydrogen Energy*, **41**, 14732 (2016).
- M. J. Larsen, I. Jiménez Morales, S. Cavaliere, J. Zajac, D. J. Jones, J. Rozière, L. Kaluža, D. Gulková, and M. Odgaard, *Int. J. Hydrogen Energy*, **42**, 7166 (2017).
- Y. Holade, R. G. da Silva, K. Servat, T. W. Napporn, C. Canaff, A. R. de Andrade, and K. B. Kokoh, *J. Mater. Chem. A*, **4**, 8337 (2016).
- J. Bai, D. Liu, J. Yang, and Y. Chen, *ChemSusChem*, **12**, 2117 (2019).
- S. S. Siwal, S. Thakur, Q. B. Zhang, and V. K. Thakur, *Mater. Today Chem.*, **14**, 100182 (2019).
- F. Fiévet, S. Ammar-Merah, R. Brayner, F. Chau, M. Giraud, F. Mammari, J. Peron, J. Y. Piquemal, L. Sicard, and G. Viau, *Chem. Soc. Rev.*, **47**, 5187 (2018).
- Y. Holade, N. Sahin, K. Servat, T. Napporn, and K. Kokoh, *Catalysts*, **5**, 310 (2015).
- I. H. Ko, W. D. Lee, J. Y. Baek, Y. E. Sung, and H. I. Lee, *Mater. Chem. Phys.*, **183**, 11 (2016).
- F. Karimi and B. A. Peppley, *Int. J. Hydrogen Energy*, **42**, 5083 (2017).
- M. Farsadrooh, M. Z. Yazdan-Abad, M. Noroozifar, H. Javadian, N. Alfi, and A. R. Modarresi-Alam, *Int. J. Hydrogen Energy*, **45**, 27312 (2020).
- L. Xu, D. Liu, D. Chen, H. Liu, and J. Yang, *Heliyon*, **5**, e01165 (2019).
- Y. Zhang, M. E. Grass, J. N. Kuhn, F. Tao, S. E. Habas, W. Huang, P. Yang, and G. A. Somorjai, *J. Am. Chem. Soc.*, **130**, 5868 (2008).
- S. Lee, C.-U. Kim, and T.-W. Kim, *J. Nanosci. Nanotechnol.*, **20**, 4525 (2020).
- R. Liu, W. D. Yang, and H. Y. Fang, *Micro & Nano Letters*, **11**, 54 (2016).
- M. C. Moraes, G. G. Junco, T. F. M. Moreira, C. J. G. Pinheiro, P. Olivi, D. Profeti, and L. P. R. Profeti, *J. Environ. Chem. Eng.*, **7**, 102922 (2019).
- F. L. S. Purgato, P. Olivi, J. M. Léger, A. R. de Andrade, G. Tremiliosi-Filho, E. R. Gonzalez, C. Lamy, and K. B. Kokoh, *J. Electroanal. Chem.*, **628**, 81 (2009).
- D. González-Quijano, W. J. I. Pech-Rodríguez, J. I. Escalante-García, G. Vargas-Gutiérrez, and F. J. Rodríguez-Varela, *Int. J. Hydrogen Energy*, **39**, 16676 (2014).
- L. W. H. Leung and M. J. Weaver, *Langmuir*, **6**, 323 (1990).
- A. Cassani, N. Tuleushova, Q. Wang, H. Guesmi, V. Bonniol, J. Cambedouzou, S. Tingry, M. Bechelany, D. Cornu, and Y. Holade, *ACS Appl. Energy Mater.*, **4**, 9944 (2021).
- R. K. Selvan, I. Perelshtein, N. Perkas, and A. Gedanken, *J. Phys. Chem. C*, **112**, 1825 (2008).

67. U. Holzwarth and N. Gibson, *Nat Nano*, **6**, 534 (2011).
68. Y. Nishida, K. Sato, T. Yamamoto, D. Wu, K. Kusada, H. Kobayashi, S. Matsumura, H. Kitagawa, and K. Nagaoka, *Chem. Lett.*, **46**, 1254 (2017).
69. S. K. Chatterjee, *X-ray Diffraction: Its Theory And Applications* (PHI Learning Pvt. Ltd.)(New Delhi) (2010).
70. L. Rao, Y.-X. Jiang, B.-W. Zhang, Y.-R. Cai, and S.-G. Sun, *Phys. Chem. Chem. Phys.*, **16**, 13662 (2014).
71. M. Ahn, I. Y. Cha, J. Cho, H. C. Ham, Y. E. Sung, and S. J. Yoo, *ACS Catal.*, **7**, 5796 (2017).
72. X. Kou et al., *Sens. Actuator B-Chem.*, **256**, 861 (2018).
73. M. J. Lambregts and S. Frank, *Talanta*, **62**, 627 (2004).
74. L. S. Zhang, J. J. Lu, S. B. Yin, L. Luo, S. Y. Jing, A. Brouzgou, J. H. Chen, P. K. Shen, and P. Tsiakaras, *Appl. Catal. B: Environ.*, **230**, 58 (2018).
75. P. Wang, Y. Wen, S. Yin, and N. Wang, *Int. J. Hydrogen Energy*, **42**, 24689 (2017).
76. G. Korotcenkov, V. Brinzari, P. Hanyš, and V. Nehasil, *Surf. Interface Anal.*, **50**, 795 (2018).
77. Y. Kang, F. Li, S. Li, P. Ji, J. Zeng, J. Jiang, and Y. Chen, *Nano Res.*, **9**, 3893 (2016).
78. J. Shim, C. R. Lee, H. K. Lee, J. S. Lee, and E. J. Cairns, *J. Power Sources*, **102**, 172 (2001).
79. A. Mondal, A. De, and J. Datta, *Int. J. Hydrogen Energy*, **44**, 10996 (2019).
80. K. Darowicki, L. Gawel, M. Mielniczek, E. Janicka, A. Zielinski, J. Mitzel, and J. Hunger, *Int. J. Hydrogen Energy*, **45**, 27551 (2020).
81. A. C. Garcia, Y. Y. Birdja, G. Tremiliosi-Filho, and M. T. M. Koper, *J. Catal.*, **346**, 117 (2017).
82. A. Xie, F. Tao, L. Hu, Y. Li, W. Sun, C. Jiang, F. Cheng, S. Luo, and C. Yao, *Electrochim. Acta*, **231**, 502 (2017).
83. C. A. Ottoni, C. E. D. Ramos, R. F. B. de Souza, S. G. da Silva, E. V. Spinace, and A. O. Neto, *Int. J. Electrochem. Sci.*, **13**, 1893 (2018).
84. F. Alcaide, G. Álvarez, P. L. Cabot, R. V. Genova-Koleva, H.-J. Grande, M. V. Martínez-Huerta, and O. Miguel, *J. Electroanal. Chem.*, **861**, 113960 (2020).
85. X. Liu, Y. Tang, M. Shen, W. Li, S. Chu, B. Shan, and R. Chen, *Chem. Sci.*, **9**, 2469 (2018).
86. H. Song, M. Luo, X. Qiu, and G. Cao, *Electrochim. Acta*, **213**, 578 (2016).
87. T. Takeguchi, A. Kunifuji, N. Narischat, M. Ito, H. Noguchi, K. Uosaki, and S. R. Mukai, *Catal. Sci. Technol.*, **6**, 3214 (2016).
88. A. A. Vedyagin, A. M. Volodin, R. M. Kenzhin, V. O. Stoyanovskii, Y. V. Shubin, P. E. Plyusnin, and I. V. Mishakov, *Catal. Today*, **293**, 73 (2017).
89. Y. Zhang, X.-R. Shi, C. Sun, S. Huang, Z. Duan, P. Ma, and J. Wang, *Mol. Catal.*, **495**, 111154 (2020).
90. W. Wang, Z. Cao, K. Liu, J. Chen, Y. Wang, and S. Xie, *Nano Lett.*, **17**, 7613 (2017).
91. F. Lei, Z. Li, L. Ye, Y. Wang, and S. Lin, *Int. J. Hydrogen Energy*, **41**, 255 (2016).
92. H. Yoshida, S. Narisawa, S.-i Fujita, L. Ruixia, and M. Arai, *Phys. Chem. Chem. Phys.*, **14**, 4724 (2012).
93. K. I. Hadjivanov and G. N. Vayssilov, *ChemInform*, **34** (2003).
94. C. Xu, Q. Li, Q. Zhang, K. Li, H. Yin, and S. Zhou, *ACS Appl. Nano Mater.*, **2**, 5086 (2019).
95. I. Yruela, S. I. Allakhverdiev, J. V. Ibarra, and V. V. Klimov, *FEBS Lett.*, **425**, 396 (1998).
96. B. Ruiz Camacho, C. Morais, M. A. Valenzuela, and N. Alonso-Vante, *Catal. Today*, **202**, 36 (2013).
97. D. K. Lambert, *Electrochim. Acta*, **41**, 623 (1996).
98. S. Beyhan, C. Coutanceau, J.-M. Léger, T. W. Napporn, and F. Kadırgan, *Int. J. Hydrogen Energy*, **38**, 6830 (2013).
99. P. Tonda-Mikiela, T. W. Napporn, C. Morais, K. Servat, A. Chen, and K. B. Kokoh, *J. Electrochem. Soc.*, **159**, H828 (2012).
100. S. Bernik and N. Daneu, *J. Eur. Ceram. Soc.*, **21**, 1879 (2001).
101. J. Banjong, A. Therdtianwong, S. Therdtianwong, S. Yongprapat, and N. Wongyao, *Int. J. Hydrogen Energy*, **45**, 2244 (2020).
102. C. C. Lima, M. V. F. Rodrigues, A. F. M. Neto, C. R. Zanata, C. T. G. V. M. T. Pires, L. S. Costa, J. Solla-Gullón, and P. S. Fernández, *Appl. Catal. B: Environ.*, **279** (2020).
103. Y. Holade, C. Morais, K. Servat, T. W. Napporn, and K. B. Kokoh, *ACS Catal.*, **3**, 2403 (2013).
104. L. Huang et al., *ACS Catal.*, **6**, 7686 (2016).
105. D. Z. Jeffery and G. A. Camara, *Electrochem. Commun.*, **12**, 1129 (2010).
106. R. S. Ferreira Jr, M. Janete Giz, and G. A. Camara, *J. Electroanal. Chem.*, **697**, 15 (2013).
107. A. C. Garcia, E. B. Ferreira, V. V. Silva de Barros, J. J. Linares, and G. Tremiliosi-Filho, *J. Electroanal. Chem.*, **793**, 188 (2017).
108. P. Hanyš, P. Janeček, V. Matolin, G. Korotcenkov, and V. Nehasil, *Surf. Sci.*, **600**, 4233 (2006).
109. D. Hiltrop, S. Cychy, K. Elumeeva, W. Schuhmann, and M. Muhler, *Beilstein J. Org. Chem.*, **14**, 1428 (2018).
110. Y. Kang, W. Wang, Y. Pu, J. Li, D. Chai, and Z. Lei, *Chem. Eng. J.*, **308**, 419 (2017).
111. M. Pagliaro, R. Ciriminna, H. Kimura, M. Rossi, and C. DellaPina, *Angew. Chem. Int. Ed.*, **46**, 4434 (2007).
112. S. B. A. Hamid, N. Basiron, W. A. Yehye, and P. Sudarsanam, *Polyhedron*, **120**, 124 (2016).
113. V. L. Oliveira, C. Morais, K. Servat, T. W. Napporn, G. Tremiliosi-Filho, and K. B. Kokoh, *J. Electroanal. Chem.*, **703**, 56 (2013).
114. Y. Holade, K. Servat, T. W. Napporn, C. Morais, J.-M. Berjeaud, and K. B. Kokoh, *ChemSusChem*, **9**, 252 (2016).
115. W. Xiao, M. A. Liutheviene Cordeiro, M. Gong, L. Han, J. Wang, C. Bian, J. Zhu, H. L. Xin, and D. Wang, *J. Mater. Chem. A*, **5**, 9867 (2017).
116. M. Neergat, V. Gunasekar, and R. Rahul, *J. Electroanal. Chem.*, **658**, 25 (2011).